Accepted for presentation in: IEEE International Conference on Communications (ICC), Glasgow, Scotland, May 2026.

Near-field Extension of Analytical Reflection Model for Large-scale mmWave IRS Geometries in 6G

Simon Häger, Marcel Kaudewitz, and Christian Wietfeld
Communication Networks Institute (CNI), TU Dortmund University, 44227 Dortmund, Germany
E-mail: {Simon.Haeger, Marcel.Kaudewitz, Christian.Wietfeld}@tu-dortmund.de

***Abstract*—In future 6G networks, large-scale apertures significantly extend the near-field (NF) to tens of meters, especially at millimeter-wave (mmWave) frequencies. This evolution challenges traditional far-field (FF)-centric communications, as users experience propagation conditions that differ markedly from FF model-driven predictions. Intelligent reflecting surfaces (IRSs) are anticipated to play a crucial role in 6G mmWave deployments by cost-effectively improving connectivity. Static IRSs, such as passive *HELIOS* geometries, have demonstrated high maturity levels in field experiments, successfully validating their capabilities. However, as shown in this work, large IRSs optimized for infinite FF behavior exhibit degraded performance in the NF, including reflection beam misalignment, broadening, magnitude reduction, and nulls. These effects can severely compromise the success of IRS-assisted 6G mmWave deployments if left unaddressed during the design phase. For this reason, we extend the analytical reflection model into the NF region. Validation through lab measurements and electromagnetic (EM) simulations confirms its enhanced accuracy in finite FF and radiative NF. The model predicts reflections at distances down to 50 cm with up to 46.5 %-pt. better correlation between the reflection patterns. These insights pave the way for optimizing NF-centric static-passive IRSs.**

***Index Terms*—near-field communications, reflecting geometry, additive architecture, physical reflection modeling, measurement.**

I. At the Heart of 6G mmWave: Near-field Communications with Large Reflectors

To meet increasing performance targets of future wireless networks, such as multi-Gbit/s peak user data rates and cell capacity, antenna technology is evolving toward extremely large antenna arrays. Combined with the move from traditional sub-6 GHz spectrum to higher mmWave (frequency range 2 (FR2)) spectrum, the FF characteristics of the emitted EM waves appear at increasing distances. In turn, the likelihood for users being in the NF becomes higher, particularly for FR2 deployments wherein obstacles effectively limit the cell size owing to poor penetration capabilities, e.g., in private network deployments within compact indoor factory (InF) halls. This is a problem because channel models are traditionally designed for FF conditions, which are vastly different from the NF, i.e., a user equipment (UE) in the NF experiences different conditions than predicted. Hence, suitable NF models need to be designed and employed for accurate propagation modeling and to achieve better wireless network performance [1–4].

Moreover, 6G is expected to adopt the novel IRS technology to reduce hardware costs and power consumption. To realize significant reflection gains that artificially boost poor non-line-of-sight (NLOS) links to line-of-sight (LOS)-like good connectivity, large reflecting surfaces, so-called large intelligent surfaces (LISs), need to be employed, featuring side lengths in the order of 10 to 100 wavelengths λ [5]. Hence, like active antennas, (semi-)passive IRS apertures and their NF regions become large [6, 7]. Particularly static-passive IRSs, i.e., non-reconfigurable reflectors, tend to be extremely large because they may be preconfigured to exhibit broad reflecting beams depending on the deployment scenario. In this context, this work will focus on the Holistic Enlightening of bLackspots with passIve reflectOr moduleS (HELIOS) IRS concept [8], which leverages custom-shaped modular reflecting geometries to achieve the desired reflection behavior (cf. Sec. II). The 3D-printed and conductively coated IRS then yields several advantages, including low cost, zero power consumption, and scalable size. Therefore, if an NF reflection model is available, network planners may better understand the impact of an IRS with desirable FF behavior on nearby UEs' connectivity. Furthermore, the IRSs may thus even be optimized to instead exhibit an optimal NF reflection behavior. Against this background, we extend our bistatic radar cross section (RCS) reflection model, applicable in the infinite FF [9], to account for finite distances down to the radiative NF region, thereby enabling more accurate propagation prognoses and NF-centric IRS customization.

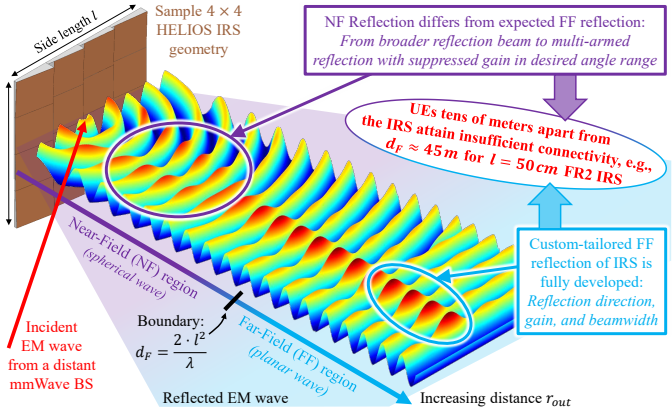

Fig. 1. Complementary use of near- and far-field reflection models enable distance-agnostic connectivity prediction and IRS customization for 6G.

The above motivation is illustrated by Fig. 1, wherein the incident EM wave from the base station (BS) impinges on a large HELIOS IRS from an oblique direction. It is then reflected with a certain beamwidth into the desired direction (here: boresight). We note that the depicted behavior loosely mirrors the behavior observed by EM simulations with commercial software [10]. It can be seen that the desired reflection behavior appears at distances larger than the Fraunhofer distance d_F. In the NF, however, the reflection differs depending on the

distance; for example, at some distances the reflection beam is broader and weaker, or even split into two beams by a null.

The remainder of this work is structured as follows. After a review of related works, Sec. II presents our existing FF reflection model for HELIOS IRSs and subsequently proposes an extension into the NF region. Sec. III evaluates the improvement in propagation prognosis accuracy of the NF-extended model against the FF model, as well as against NF EM simulations and laboratory measurements. Last, we summarize our key results and provide an outlook on future work in Sec. IV.

II. Toward NF IRS Reflection Models for 6G

This section first highlights in Sec. II-A, how propagation models with IRS support require knowledge of the reflection of flat metallic surfaces. Sec. II-B then introduces geometry-driven HELIOS IRSs and the corresponding far-field reflection model. It is then extended into the NF region in Sec. II-C.

A. Foundations: Modeling IRS-based Propagation Paths based on the Reflection Characteristics of Flat Metal Plates

Accurate user connectivity prognoses in far- or near-fields depend on the propagation model considering individual pathways for the EM waves. This work focuses on the dominant paths, for example, the LOS path whose received power P_{RX} from the transmitter (TX) to the receiver (RX) is described by

$$P_{\text{RX}} = \frac{P_{\text{TX}} \cdot G_{\text{TX}} \cdot G_{\text{RX}} \cdot \lambda^2}{(4\pi)^2 \cdot d_{\text{TX,RX}}^2}, \tag{1}$$

which depends on the free-space distance $d_{\text{TX,RX}}$, wavelength λ, transmit power P_{TX}, and antenna gains $G_{\text{TX}}, G_{\text{RX}}$ of the transceivers [11, Ch. 2.1]. Obstacles such as building walls result in additional loss, which is particularly high for mmWaves, such that an IRS shall be used to provide a superior link quality based on reflection gain σ_{IRS} from TX to RX direction. In the literature, σ_{IRS} is referred to as the bistatic RCS with unit m^2 (logarithmic unit: dBsm). The received power P_{RX} along this virtual LOS link is described by the radar equation

$$P_{\text{RX}} = \frac{P_{\text{TX}} \cdot G_{\text{TX}} \cdot G_{\text{RX}} \cdot \sigma_{\text{IRS}} \cdot \lambda^2}{(4\pi)^3 \cdot d_{\text{TX,IRS}}^2 \cdot d_{\text{IRS,RX}}^2}, \tag{2}$$

where $d_{\text{TX,IRS}}$ and $d_{\text{IRS,RX}}$ describe the distances between the respective transceivers and the IRS position [11, Ch. 2.1]. For decades, in the scope of designing better radars or objects that avoid detection through such systems, numerous works have derived the FF RCS of arbitrarily-shaped geometries as functions of azimuth angle of incidence (AoI) ϕ_{in}, elevation AoI θ_{in}, azimuth angle of departure (AoD) ϕ_{out}, and elevation AoD θ_{out}. For complex shapes like curved metasurfaces [12] and our HELIOS IRS geometry [9], one coherently sums up the reflection of simpler shapes, i.e., small flat plates. Based thereon, with little modification, reflection models for synthetic, semi-passive IRSs featuring flat sub-wavelength unit cells have already been derived, e.g., in [13–16]. Although designed for the infinite far-field, these models exhibit a high accuracy for distances exceeding the Fraunhofer distance [17]

$$d_F = 2 \cdot l^2 / \lambda, \tag{3}$$

where l is the largest side length of the reflecting surface panel.

As 6G research increasingly emphasizes NF rather than FF conditions, we revisit the reflection behavior of flat metallic plates, extending the analysis into the radiating NF region ($d_F \geq r_{out} \geq 0.62\sqrt{l^3/\lambda}$) [1]. One critical effect to capture is the loss-inducing broadening of the reflection. Both measurements [18] and electromagnetic simulations [19] consistently show that, unlike in the FF, reflections from flat metallic plates in the radiative NF are not confined to narrow angular lobes but spread across a broader angular region in both azimuth and elevation space. Hence, users may be outside the reflection lobe in the FF but be served at the same angle within the NF of the reflector. With increasing distance, however, the beam shapes into the well-known far-field behavior. The opposite behavior may also occur if the user is too close to the surface, i.e., in the reactive NF, and thus too close for the reflection beam to have formed. Hence, a user may also be served very poorly in the NF, while there would be an excellent reflection in the FF.

Other NF characteristics largely resemble their FF counterparts. For example, the peak FF RCS is defined by [11, Ch. 6]

$$\sigma = \lim_{r_{out} \to \infty} 4\pi \cdot r_{out}^2 \cdot \frac{|E_s|^2}{|E_0|^2}, \tag{4}$$

where $|E_0|$ and $|E_s|$ are the magnitudes of the incident and scattered E-fields, and r_{out} is the (infinite) radius. In the NF, σ is still proportional to the square of the radius [18], thus allowing for extension of the RCS and radar equation concepts into the NF. Moreover, the impact of the reflecting surface size and wavelength is overall similar to that in the FF. However, nulls emerge at characteristic NF distances r_{out} (cf. $d_{\text{IRS,RX}}$), in turn depending on the operating frequency [18] and the flat surface's dimensions. There are specialized NF reflection models that have been developed for the monostatic reflection case [20], i.e., limited to $(\phi_{out}, \theta_{out}) = (\phi_{in}, \theta_{in})$, and thus not applicable to IRSs which shall reflect into intelligently selected directions of interest, i.e., $(\phi_{out}, \theta_{out}) \neq (\phi_{in}, \theta_{in})$.

To the best of the authors' knowledge, there is no bistatic NF reflection formula for reflecting surfaces, likely because the NF case has little relevance in the field of radar science. Thus, under the assumption of broadband and multi-antenna communications, which mitigate the previously described nulls in NF reflections [19], our contribution in Sec. II-C will extend the bistatic FF reflection model toward the NF without modeling frequency-specific fades at certain distances from the IRS panel. Considering that it is likely that, for example, only the UE but not the BS shall be close to the IRS, it seems even more valid to entertain this notion. However, for the far-field model from Sec. II-B to become applicable at short distances, small reflecting surfaces need to be considered, cf. Fraunhofer distance definition in Eq. (3). Therefore, similar to how the FF RCS of complex 3D geometries is calculated based on numerous flat patches, we model the NF reflection of a large IRS in Sec. II-B based on the FF reflection of numerous contained patches. This resembles a recent 'Piecewise FF' approach for modeling of NF communication channels with an extremely large antenna array [1]. Importantly, we show that this approach captures the key NF effects on the reflection beam in the radiative NF.

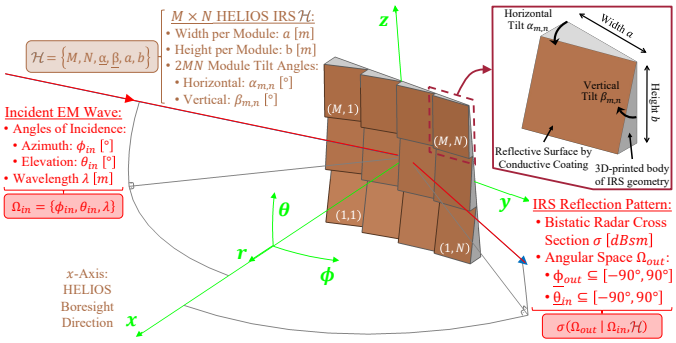

Fig. 2. Overview of employed HELIOS IRS concept for an arbitrary 3×4 geometry $\mathcal{H}$ along with an introduction of its key parameters.

B. Far-field Reflection of HELIOS IRS Geometries

We recently introduced a physical optics (PO)-based reflection model for our HELIOS IRS, which was shown to accurately predict its overall bistatic RCS pattern $\sigma\left(\Omega_{out}|\Omega_{in}, \mathcal{H}\right)$ in the hemisphere Ω_{out} defined by all azimuth and elevation reflection angles $\phi_{out}, \theta_{out} \in \Omega_{out} = [-90°, -90°]$ [9]. The model requires a description of the incident wave provided by set Ω_{in}, containing azimuth and elevation **AOI!**s (**AOI!**s) ϕ_{in}, θ_{in}, and wavelength λ. Another essential input for the FF reflection model is the IRS geometry, denoted by $\mathcal{H}$: As depicted in Fig. 2, a HELIOS reflector consists of $M \times N$ modules, each with a footprint of $b \times a$ (height $\times$ width), having an impact on the directivity of the module's reflection, i.e., its beamwidth and gain. Each module may further be tilted horizontally by angle $\alpha_{m,n}$ around the z-axis, and vertically by angle $\beta_{m,n}$ around the y-axis, with $m = 1, \ldots, M$ and $N = 1, \ldots, N$. Thus, each module has a protrusion depth $d_{m,n}$ of $b \cdot \tan|\beta_{m,n}| + a \cdot \tan|\alpha_{m,n}| + h_{m,n}$. According to the natural law of reflection, these $2MN$ tilt parameters redirect the incident wave into MN directions $(2\alpha_{m,n} - \phi_{in}, 2\beta_{m,n} - \theta_{in})$. There are further geometry parameters that can be used to optimize the reflection behavior, such as common horizontal and vertical inter-module spacings d_y, d_z, and module height offsets $h_{m,n}$ (all $\geq 0\,\mathrm{m}$), which are neither depicted in Fig. 2 nor used in this work for brevity. The parameters are optimized by a genetic algorithm to meet a desirable FF reflection behavior. The identified geometry is then 3D-printed with a robust filament, followed by spray-coating of the tilted surfaces using a copper-based conductive varnish [8].

Against this introduction of the HELIOS architecture, we briefly recapitulate the reflection model below, i.e., we describe how it determines the RCS σ at an arbitrary observation direction $(\phi_{out}, \theta_{out})$ in the infinite far-field $(r_{out} \to \infty)$ [9]:

$$\sigma\left(\phi_{out}, \theta_{out}\right) = \sum_{m=1}^{M} \sum_{n=1}^{N} \left(\sqrt{\sigma_{m,n}} \cdot e^{j \cdot \psi_{m,n}}\right)^2 \text{ with } \quad (5)$$

$$\sigma_{m,n} = 4\pi \left(\frac{a^r \cdot b^r}{\lambda} \cdot T \cdot \frac{\sin Y}{Y} \cdot \frac{\sin Z}{Z}\right)^2 \text{ using } \quad (6)$$

$$T\left(\phi_{out}, \theta_{out}\right) = -\cos\theta_i^r \sin\theta_o^r \sin\phi_o^r - \cos\theta_i^r \cos\phi_o^r + \cos\theta_o^r \sin\theta_i^r \sin\phi_i^r, \quad (7)$$

$$Y\left(\phi_{out}, \theta_{out}\right) = \frac{\pi \cdot a^r}{\lambda} \cdot \left(\sin\phi_o^r \cos\theta_o^r + \sin\phi_i^r \cos\theta_i^r\right), \quad (8)$$

$$\text{and} \quad Z\left(\theta_{out}\right) = \frac{\pi \cdot b^r}{\lambda} \cdot \left(\sin\theta_o^r + \sin\theta_i^r\right). \quad (9)$$

Moreover, in the prior Eqs. (6) to (9), the following module-specific geometric transformations are leveraged for brevity:

$$\phi_i^r = \phi_{in} - \alpha_{m,n}, \quad \phi_o^r = \phi_{out} - \alpha_{m,n} \quad (10)$$

$$\theta_i^r = \theta_{in} - \beta_{m,n}, \quad \theta_o^r = \theta_{out} - \beta_{m,n} \quad (11)$$

$$a^r = a \cdot \sqrt{1 + \tan^2\left(\alpha_{m,n}\right)}, \quad b^r = b \cdot \sqrt{1 + \tan^2\left(\beta_{m,n}\right)} \quad (12)$$

Last, it remains to mention that $\psi_{m,n}$ describes the phase offset between the center of the reflecting surface $P_{m,n}$ (cf. Eq. (13)) of module (m, n) and the IRS origin $[0, 0, 0]^T$.

$$P_{m,n} = \begin{bmatrix} \frac{a}{2} \cdot |\tan\alpha_{m,n}| + \frac{b}{2} \cdot |\tan\beta_{m,n}| + h_{m,n} \\ \frac{2n - 1 - N}{2} \cdot a + \frac{2\,(n-1) - (N-1)}{2} \cdot d_y \\ \frac{2m - 1 - M}{2} \cdot b + \frac{2\,(m-1) - (M-1)}{2} \cdot d_z \end{bmatrix} \quad (13)$$

We note that some configurations of the geometry result in self-shadowing between individual modules. This reduces the effective reflecting surface size, such that the model trims the surface size $b^r \times a^r$ to the effective reflecting surface patch, as described in detail in [9]. Accordingly, the effective center position $P_{m,n}$ of the affected modules' is also adjusted.

C. Reflection Model Extension to the Near-Field

First, we define the Cartesian NF observation coordinate P_C with respect to the IRS origin. P_C shall be equivalently represented by the spherical coordinates $[r_{out}, \phi_{out}, \theta_{out}]$ via

$$P_C = \begin{bmatrix} X_C \\ Y_C \\ Z_C \end{bmatrix} = r_{out} \cdot \begin{bmatrix} \cos\phi_{out} \cos\theta_{out} \\ \sin\phi_{out} \cos\theta_{out} \\ \sin\theta_{out} \end{bmatrix}. \quad (14)$$

Against this background, one should ideally use a NF reflection model to determine each module's reflection gain $\sigma_{m,n}$ with parameters radius $r_{m,n}$, azimuth reflection angle $\phi_{m,n}$, and elevation reflection angle $\theta_{m,n}$ between reflection center $P_{m,n}$ and the NF observation coordinate P_C, as shown

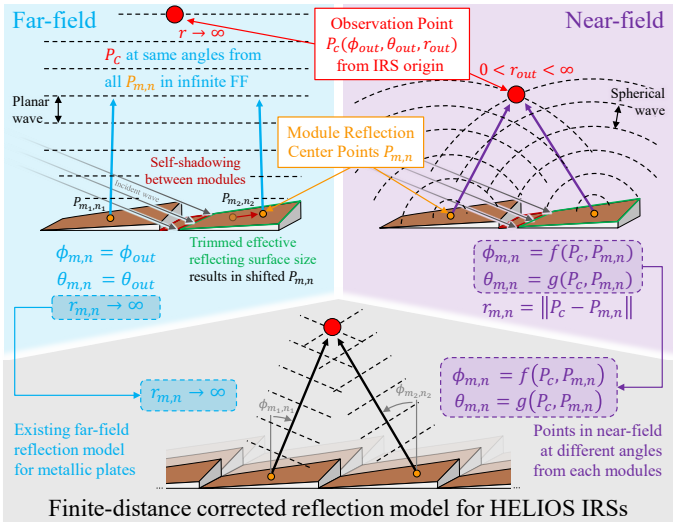

Fig. 3. Proposed NF IRS reflection model *(bottom)*, combining the infinite FF reflection model for geometry-defined IRSs *(top left)* with individual reflection angles $(\phi_{m,n}, \theta_{m,n})$ from each module's reflection center $P_{m,n}$ to the NF position P_C *(top right)*.

at the top right of Fig. 3. The reflections of each module would then be combined by coherent summation as in Eq. (5). However, as described in Sec. II-A, there is no formula for the NF reflection of metallic rectangular plates, as utilized in Eq. (6) of the FF model. Having observed a successful finite-distance correction of a FF model for massive antenna arrays in our literature review, this approach is transferred to our geometry-driven IRS, as depicted in Fig. 3: Following the 'Piecewise FF' approach from [1], we employ our FF model for the reflection of each HELIOS module (cf. Eq. (6)) to extend it into the NF. As shown at the top left of Fig. 3, the FF model operates under the assumption that P_C is infinitely far away from the IRS, i.e., $r_{m,n} \to \infty$, such that all reflection observation angles are identical, i.e., $\phi_{m,n} = \phi_{out}$ and $\theta_{m,n} = \theta_{out}$ for all MN modules. This is changed in this work as sketched at the bottom of Fig. 3: Whereas $r_{m,n}$ remains infinite because this parameter does not exist in the FF equation, we consider that the angles from the effective reflection centers of the modules to the NF observation differ:

$$\tan\phi_{m,n} = \frac{\Delta Y_{m,n}}{\Delta X_{m,n}} \text{ and } \tan\theta_{m,n} = \frac{\Delta Z_{m,n}}{\sqrt{\Delta X_{m,n}^2 + \Delta Y_{m,n}^2}}, \quad (15)$$

where $\Delta X_{m,n}, \Delta Y_{m,n}, \Delta Z_{m,n}$ are the elements of vector

$$\Delta P_{m,n} = P_C - P_{m,n} = [\Delta X_{m,n}\ \Delta Y_{m,n}\ \Delta Z_{m,n}]^T . \quad (16)$$

For this reason, we denote Eqs. (15) to (16) in Fig. 3 using $\phi_{m,n} = f(P_C, P_{m,n})$ and $\theta_{m,n} = g(P_C, P_{m,n})$. Importantly, having defined the observation point P_C with dependence on r_{out} in Eq. (14), it is straightforward to determine that it holds

$$(\phi_{m,n}, \theta_{m,n}) \xrightarrow{r_{out}\to\infty} (\phi_{out}, \theta_{out}) . \quad (17)$$

Therefore, the proposed NF-extended reflection model smoothly transitions to the infinite FF model for large r_{out}.

III. Experiments-driven Model Validation

This section evaluates the proposed NF extension of the FF IRS reflection model. First, Sec. III-A assesses the performance improvement over the FF model by comparing it against EM simulations for a simple reflector setup. In Sec. III-B, we custom-tailor a conventional FF-specific HELIOS IRS, introduce the laboratory measurement methodology, and then evaluate our NF-extended model against the attained data. Last, Sec. III-C outlines the benefits of employing the proposed model for NF-tailored IRS customization.

A. Validation against EM Simulations

This section considers an arbitrarily-selected simple, i.e., non-optimized, reflector structure as shown in Fig. 4a. It consists of two modules in a row (1×2 arrangement) and only a fixed azimuth tilt angle α of $-22.5°$ is employed. The incident EM wave impinges from $\phi_{in} = -45°$. Subsequently, we study the reflection characteristics of the NF-extended model (from Sec. II-C), infinite FF model (from [9]), and EM simulations (using [10]) in the horizontal plane for different azimuth reflection angles ϕ_{out} and distances r_{out} from the reflector. We note that whereas the NF RCS in the EM simulations are directly available for (infinite) FF solvers, NF solvers return only the E-field magnitude in relation to the incident EM wave magnitude. Hence, the RCS is then attained per definition by multiplying with $4\pi r_{out}^2$, cf. Eq. (6).

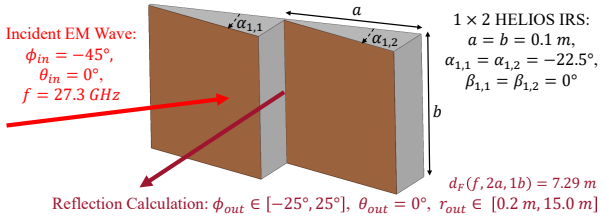

(a) Simple test scenario and reflector geometry for validation in (b)–(d).

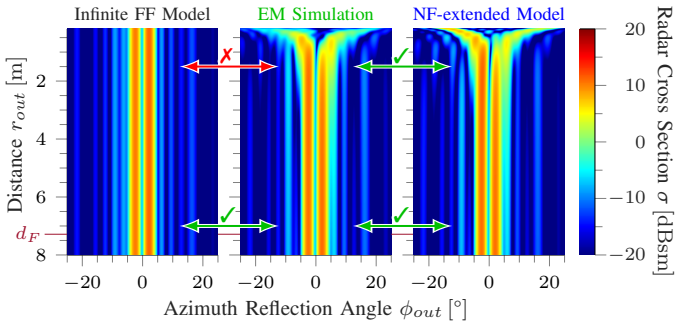

(b) Comparison of infinite FF model, simulation, and NF-extended model.

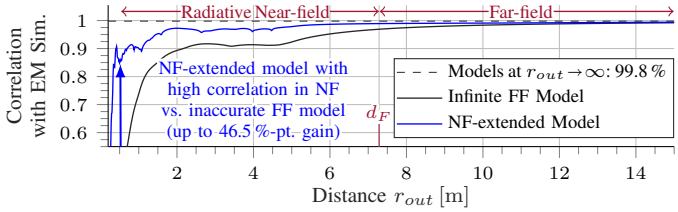

(c) Correlation between simulation and the respective analytical models.

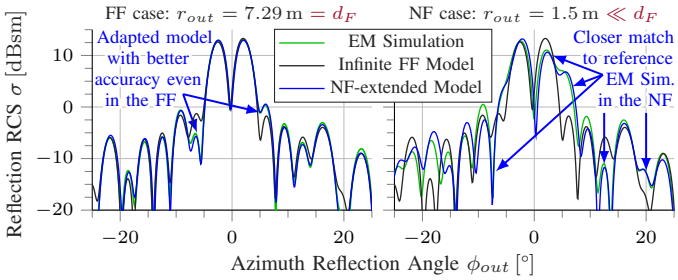

(d) Comparison of horizontal-plane reflection pattern at selected distances.

Fig. 4. Validation of improved performance in vicinity of HELIOS IRS using proposed NF extension over the FF model, as corroborated by EM simulations.

Fig. 4b depicts the RCS patterns for distances of up to 8 m, i.e., just surpassing $d_F = 7.29\,\text{m}$. It can be seen that the infinite FF model, shown in the left column, is independent of distance. As a consequence, it matches EM simulation results, given in the middle column, only at large distances ($r_{out} \geq d_F$). At small ranges, the simulated reflection beam broadens and a null appears in the center direction $\phi_{out} = 0°$. Now, considering the proposed NF model extension, as shown on the right side, we find that the reflection behavior is accurately presented in both FF and NF.

We consider the respective range-specific correlations of the two analytical models' beam patterns ($\phi_{out} \in [-25°, 25°]$) and

the EM simulation results in Fig. 4c. In the infinite FF, the FF model and EM simulations exhibit near-perfect correlation with a value of 99.78 %, which is depicted by a dashed line for reference. The missing 0.22 % are induced by, e.g., limitations of the underlying PO-based modeling approach [9]. For smaller distances, however, the correlation between FF model and EM simulation deteriorates and even gets negative for $r_{out} \leq 0.31\,\mathrm{m}$. In contrast, the proposed NF-extended model – with high correlation of at least 86.02 % – remains close to the established performance reference down to a distance of 53 cm, being the lower bound of the radiative NF.

The reflection patterns are directly compared in Fig. 4d for two distances: At distance $r_{out} = d_F = 7.3\,\mathrm{m}$, as shown on the left side, all three methods yield very similar RCS patterns as expected for this FF case. However, the NF extension describes the reflection outside the two main lobes more accurately, such that it is better correlated by 2.01 %-pt., cf. Fig. 4c. The right subfigure in Fig. 4d considers the NF distance $r_{out} = 1.5\,\mathrm{m}\,(\approx 0.2 d_F)$ for which the NF model has a high correlation of 95.3 % with the EM simulation, and thus outperforms the FF model by a 9.78 %-pt. margin. Accordingly, the reflection patterns of EM simulation and NF-extended model match well near the two main lobes, whereas the FF model yields errors of up to 10 dB. Fig. 4 has thus successfully demonstrated the functionality and performance gains of the proposed model extension into the NF region.

B. Validation against Measurements

Considering the prior simulation-based validation for a simple geometry, this section provides a complementary experimental assessment with a complex real HELIOS geometry. Sec. III-B1 briefly describes IRS FF design requirements and the attained custom panel. Subsequently, Sec. III-B2 presents the laboratory measurement setup. Sec. III-B3 discusses the measurement results featuring comparisons with both FF and NF predictions from EM simulations and the proposed model.

1) Custom-tailored Static-passive FF Reflector: The full list of IRS design requirements is provided in Tab. I. In particular, the operating frequency and AoIs from the previous section are reused; however, the reflection is now reflected toward the angular range $\phi_{out} \in [25°, 35°]$, based on the center azimuth reflection direction $\phi_{o,c} = 30°$ and horizontal beamwidth $\Delta\phi_o = 10°$ parameters. Again, it shall primarily serve users at the same height as we set center elevation direction $\theta_{o,c} = 0°$ with a narrow vertical beamwidth $\Delta\theta_o = 3°$. The reflector features 16 modules (4×4 arrangement) over an overall footprint area of $29.7\,\mathrm{cm} \times 29.7\,\mathrm{cm}$, which is slightly smaller than the quiet zone in the test chamber, cf. Sec. III-B2. The reflector tilt parameters $(\alpha_{m,n}, \beta_{m,n})$ are determined by a genetic algorithm set to maximize the minimum in-beam RCS σ in the target angular reflection space [21], based on the infinite FF model [9]. For higher performance, row and column symmetries are used such that only eight $(M + N)$ instead of 32 $(2MN)$ parameters need to be identified [21]. As a result, the IRS described in Fig. 5 was selected and produced [8, 9].

TABLE I. DESIGN CONSTRAINTS FOR THE HELIOS IRSS.

	Parameter	Description/Value
Input	Carrier frequency	$f = 27.3\,\mathrm{GHz}$
	Azimuth angle of incidence	$\phi_{in} = -45°$
	Elevation angle of incidence	$\theta_{in} = 0°$
FF Output	Center azimuth reflection angles	$\phi_{o,c} = 30°$
	Horizontal beamwidth	$\Delta\phi_o = 10°$
	Center elevation reflection angle	$\theta_{o,c} = 0°$
	Vertical beamwidth	$\Delta\theta_o = 3°$
	Angular resolution	$\Delta\phi_{o,res} = \Delta\theta_{o,res} = 0.1°$
Shape	Overall footprint size	$N \cdot a = M \cdot b = 29.7\,\mathrm{cm}$
	Module arrangement	$M = N = 4$
	Module footprint	$a = b = 6.76\lambda$
	Symmetric surface tilts	$K = M + N = 8$ parameters

$(\alpha_{m,n}, \beta_{m,n})$	$n=1$	$n=2$	$n=3$	$n=4$
$m=4$	(−10.69°, −2.00°)	(−7.89°, −2.00°)	(−5.39°, −2.00°)	(−7.14°, −2.00°)
$m=3$	(−10.69°, −0.00°)	(−7.89°, −0.00°)	(−5.39°, −0.00°)	(−7.14°, −0.00°)
$m=2$	(−10.69°, +0.07°)	(−7.89°, +0.07°)	(−5.39°, +0.07°)	(−7.14°, +0.07°)
$m=1$	(−10.69°, +2.00°)	(−7.89°, +2.00°)	(−5.39°, +2.00°)	(−7.14°, +2.00°)

Custom Module Tilt Angle Selection with Symmetry Conditions

FF HELIOS IRS

Fig. 5. Pole-mounted passive HELIOS IRS and full configuration, fostering reproduction of presented measurement, EM simulation, and model results.

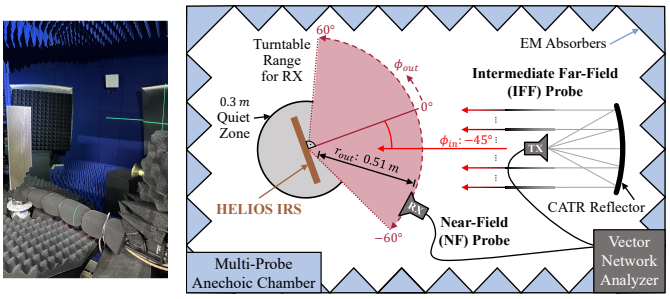

(a) IRS under test. (b) Top-view sketch of laboratory setup.

Fig. 6. Overview of near-field measurements of HELIOS IRS reflection.

TABLE II. LABORATORY MEASUREMENT SETUP DETAILS.

Parameter	Description/Value
Transmit power	$P_{TX} = -14.4\,\mathrm{dBm}$
Antenna gains	$G_{TX} = 9.5\,\mathrm{dBi}, G_{RX} = 15.1\,\mathrm{dBi}$
AoIs (az., el.)	$\phi_{in} = -45°, \theta_{in} = 0°$
Frequencies	$f = 27.3\,\mathrm{GHz}$; $f \in [24\,\mathrm{GHz} : 10\,\mathrm{MHz} : 42\,\mathrm{GHz}]$
Incident wave at IRS	Indirect far-field using CATR reflector
Reflected wave at RX	Near-field of IRS with $r_{out} = 0.51\,\mathrm{m}$
Measured angles	$\phi_{out} \in [-60° : 0.5° : 60°]$, $\theta_{out} = 0°$
Performance metric	Path Gain (in dB), for hor. and vert. polarization

2) Measurement Methodology: Bistatic reflection measurements under suppressed multipath effects are conducted in a multi-probe compact antenna test range (CATR) anechoic chamber (Keysight F9651A), as shown in Fig. 6. The CATR reflector is fed by a TX feed horn antenna, thereby realizing an intermediate far-field illumination of the IRS within a quiet zone area with side length of 30 cm. An RX probe is used to measure the bistatic FF to NF reflection pattern with a radius of about 0.5 m. It is mounted on a turntable platform, facilitating systematic measurements of reflection patterns at different angles ϕ_{out} with an angular resolution of 0.5°. A sensitive vector network analyzer (VNA), i.e., Keysight N5247B, is employed to measure the angular reflected power profile along both horizontal and vertical polarizations at 27.3 GHz, as

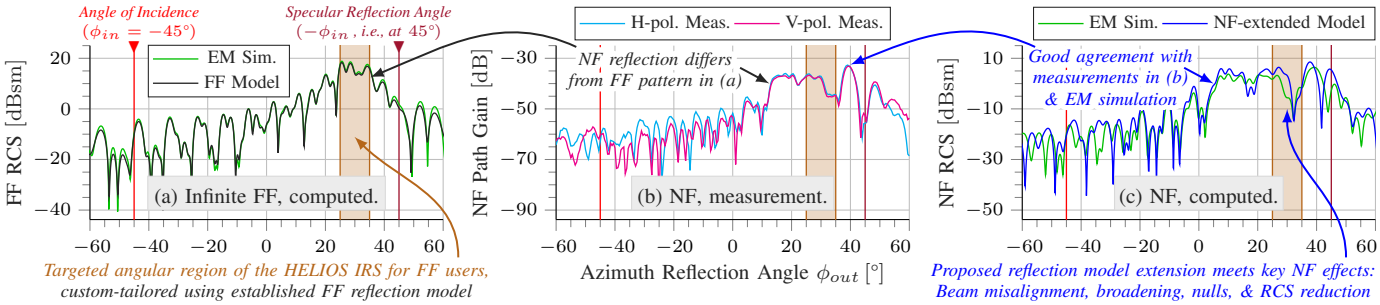

Fig. 7. Measured NF reflection of HELIOS IRS differs from the FF model used in the design stage and is better described by the proposed NF-extended model.

part of a measurement campaign for the 24 GHz to 42 GHz spectrum range, containing the major global cellular mmWave communication bands, with a 10 MHz resolution [22].

The main performance metric of these measurements is the path gain (i.e., inverse of path loss), which relates the measured received power level to the transmit power level. As it is available over an 120° angular range, we can assess the frequency-specific angular NF reflection pattern of the IRS. The above-described measurement details are summarized in Tab. II.

3) Comparing Measurements, Simulations, and Models: Our analysis in Fig. 7 compares the NF measurement data against EM simulations (using [10]), the infinite FF reflection model (from [9]), and this work's NF-extended reflection model. The combination of simulation, measurement, and model allows us to underline the impact of using a preconfigured FF IRS in NF conditions while again validating the proposed reflection model extension as follows: We find in Fig. 7a that the FF model-based custom IRS serves the intended angular region with a broad beam with 13.3–18.3 dBsm. The reflection behavior of the IRS design, determined via 17,680 RCS calculations during the HELIOS optimization process, is validated by the computationally intensive EM simulations (99.3 % correlation). Outside the IRS's beam ($|\phi_{out}| \to 90°$), differences increase due to the model's PO assumption, cf. [9].

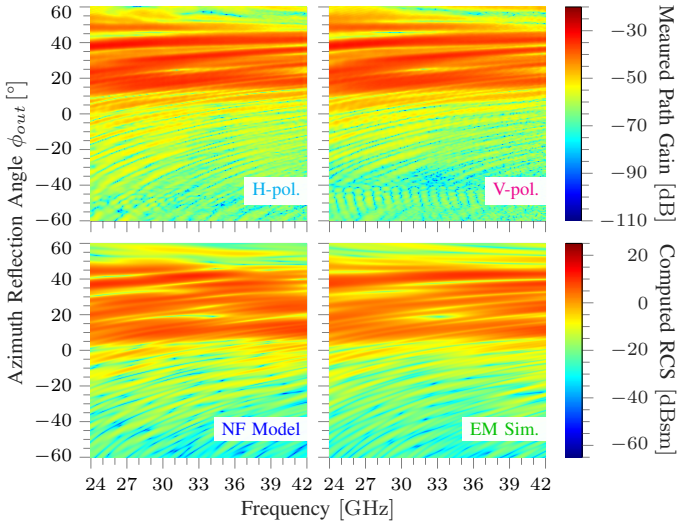

Fig. 8. Frequency-agnostic match between proposed model, EM simulations, and polarization-specific measurements: *(top)* Horizontal and vertical polarized power measurements, *(bottom)* simulation- and model-based RCS.

The measured reflection is shown in Fig. 7b, yielding little impact by polarization near the main reflection lobes. It can be seen that the reflection beam is now broadened, misaligned, and exhibits a reflection null in the intended angular range. This is also confirmed by EM simulations and the NF-extended model in Fig. 7c. Additionally, when comparing the attained NF RCS with the FF RCS in Fig. 7a, we further find that the peak reflection is approximately 10 dB weaker. Together, these four reflection behavior changes underline that, in the future, static HELIOS IRSs need to be customized based on an NF model if their service area is at least partially in the NF.

Back to Fig. 7c, we note that EM simulations, NF model, and measurements differ slightly from each other. Reasons for this could be remaining multipath propagation, measurement setup inaccuracies (regarding ϕ_{out}, r_{out}), and that the incident wave is not entirely planar [21, 22]. While both computational methods match their respective set of aspects from the measurements in Fig. 7b, we observe that the EM simulations are a slightly better match (80.2 % vs. 75.7 % correlation with V-pol. data). However, this does not imply that the proposed NF-model performs inadequately. On the contrary, when accounting for the fact that the FF RCS equations for metal plates are used with finite-distance corrections for a lack of NF equations, the accuracy at such a short distance of 0.51 m (placing it in the reactive NF) is surprisingly high, considering that we have found in Sec. III-A that it is more suitable in the radiative NF (with larger r_{out} than in the reactive NF).

Last, we briefly note with reference to Fig. 8 that the proposed NF-extended model is also found to be accurate at different frequencies. Hence summarize the results of Figs. 7 to 8 are summarized as follows: Regardless of frequency, the NF model is faster than EM simulations and more accurate in the radiative NF; considering the results of Sec. III-A, it is even more accurate for distances larger than the Fraunhofer distance d_F. Hence, it shall serve as a basis for future HELIOS IRS customizations, regardless of frequency and UE-IRS distance.

C. Potential Analysis of NF-tailored Static-passive IRSs

After validating the accuracy of the proposed NF-extended reflection model against EM simulations and measurements, and demonstrating its performance gains over the infinite FF model, we now illustrate its applicability to the customization of static-passive HELIOS IRSs. The design constraints listed in Tab. I are reused; however, the target radius is set to 3.0 m, i.e.,

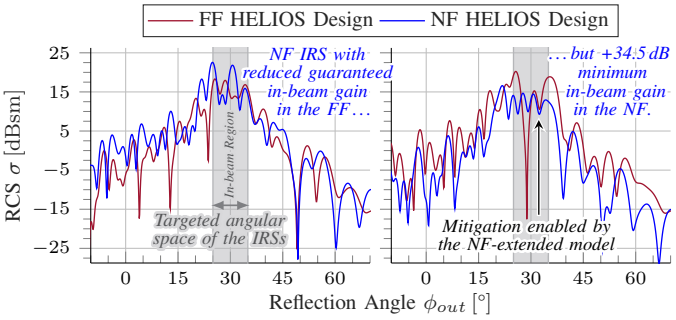

(a) UE in FF: $r_{out} \to \infty$ (b) UE in NF: $r_{out} = 3.0\,\mathrm{m}$

Fig. 9. Horizontal reflection pattern slices of FF- and NF-centric custom mmWave IRSs in the *(left)* far-field and *(right)* near-field. Using the proposed model, NF UEs are served with a minimum in-beam gain of 8.9 dBsm (and peak gain of 14.7 dBsm), instead of suffering an up to 34.5 dB reduction of guaranteed in-beam gain from NF-induced nulls occurring for the FF IRS.

$r_{out} \approx 0.2 d_F$. The resulting reflection patterns in both the near- and far-field can thus be directly compared with those of the FF-optimized IRS introduced in Sec. III-B and shown in Fig. 5.

We first consider the performance of both IRSs in the FF, as shown for the horizontal RCS slice in Fig. 9a. Whereas the FF-centric IRS exhibits a minimum in-beam RCS of 10.15 dBsm in the $3° \times 10°$ (vert. $\times$ hor.) reflection space, the NF-centric design may only guarantee a reduced reflection level. Therefore, a relative loss in the design objective value (cf. [21]) is incurred with the NF IRS in the far-field, however, this is reasonable because the NF IRS was not explicitly custom-tailored for the considered long-range distance. However, the situation reverses in the near-field, as intended: Specifically, the FF reflector geometry in Fig. 9b exhibits an undesirable null in the target reflection space with a minimum in-beam RCS of −25.59 dBsm, which is in line with the effects observed in Secs. III-A to III-B as it was not designed for such short ranges. In contrast, the NF HELIOS variant does not exhibit a null and shapes a reflection beam with at least 8.87 dBsm in the targeted angular region. Overall, a 34.5 dB improvement of guaranteed in-beam reflection gain is realized, clearly highlighting the advantages of the proposed reflection model extension, which enables accurate IRS design from the finite far-field down to the radiative near-field regime.

IV. Conclusions and Outlook

This manuscript has presented an NF extension of an analytical reflection model for geometric IRSs, which previously described only the bistatic RCS in the infinite FF. Laboratory measurements and EM simulations confirm that the proposed model enables more accurate predictions of mmWave IRS reflection characteristics for UEs at tens of meters down to 0.5 m from the reflecting panel. Our results also demonstrate that NF reflections differ markedly from conventional FF behavior: the reflected beam is misaligned, weaker, broader, and exhibits undesired nulls in the target direction. These findings underline that IRS designs optimized for FF conditions may be unsuitable when UEs are predominantly positioned near the surface. As showcased, future work will thus employ the NF-extended reflection model to design static-passive HELIOS IRS geometries with tens of dB improved connectivity for nearby users.

Acknowledgment

This work has been funded in parts by the German Federal Ministry of Research, Technology and Space (BMFTR) in the course of the *6GEM* Research Hub under the grant number 16KISK038, the *6GEM+* Transfer Hub under the grant number 16KIS2412, and the *PANGOLIN Networks* project under the grant number 16KIS2357. The authors thank Keysight Technologies for supporting the laboratory HELIOS IRS measurements in Sec. III-B2.

References

[1] M. Cui and L. Dai, "Near-field wideband beamforming for extremely large antenna arrays," *IEEE Trans. Wirel. Commun.*, vol. 23, no. 10, pp. 13 110–13 124, Oct. 2024.

[2] Z. Wang, H. Wu, Y. Chen, and L. Lu, "New paradigm for unified near-field and far-field wireless communications," *IEEE Network*, vol. 39, no. 6, pp. 112–118, Nov. 2025.

[3] Z. Ma, G. Steinböck, and H. Asplund, "Assessing the necessity of modeling non-planar wavefronts for large arrays with ray-tracing simulation," in *Proc. EuCAP Conf.*, Apr. 2025, IEEE.

[4] Y. Liu, C. Ouyang, Z. Wang, J. Xu, X. Mu, and A. L. Swindlehurst, "Near-field communications: A comprehensive survey," *IEEE Commun. Surv. Tutor.*, vol. 27, no. 3, pp. 1687–1728, Jun. 2025.

[5] S. Häger, M. Kaudewitz, F. Schmickmann, S. Böcker, and C. Wietfeld, "Field performance evaluation of a mechatronic reflector system in a private mmWave network environment," *IEEE Open J. Commun. Soc.*, vol. 6, pp. 5005–5029, Jun. 2025.

[6] X. Mu, J. Xu, Y. Liu, and L. Hanzo, "Reconfigurable intelligent surface-aided near-field communications for 6G: Opportunities and challenges," *IEEE Veh. Technol. Mag.*, vol. 19, no. 1, pp. 65–74, Mar. 2024.

[7] RIS TECH Alliance (RISTA). (2025, Apr.) 6G near-field technologies. White Paper, Version 2.0. DOI: 10.12142/FuTURE.202504001.

[8] S. Häger, M. Danger, K. Heimann, Y. Gümüs, S. Böcker, and C. Wietfeld, "Custom design and experimental evaluation of passive reflectors for mmWave private networks," in *Proc. IEEE LANMAN Symp.*, Jul. 2024, best paper award.

[9] S. Häger, S. Böcker, and C. Wietfeld, "Reflection modeling of modular passive IRS geometries," *IEEE Wirel. Commun. Lett.*, vol. 14, no. 5, pp. 1366–1370, May 2025.

[10] Ansys, Inc. High frequency simulation software (HFSS). [Online]. Available: https://www.ansys.com/hfss

[11] D. E. Kerr, *Propagation of Short Radio Waves*, 1st ed., ser. Electromagnetics and Radar. Inst. Eng. & Technol. (IET), Apr. 1987.

[12] A. P. Ganesh, W. Khawaja, O. Ozdemir, I. Güvenç, H. Nomoto, and Y. Ide, "Propagation measurements and coverage analysis for mmWave and sub-THz frequency bands with transparent reflectors," in *Proc. IEEE VTC-Spring Conf.*, Aug. 2023.

[13] Ö. Özdogan, E. Björnson, and E. G. Larsson, "Intelligent reflecting surfaces: Physics, propagation, and pathloss modeling," *IEEE Wirel. Commun. Lett.*, vol. 9, no. 5, pp. 581–585, May 2020.

[14] M. Wei, D. Jianwu, C. Yijun, and Y. Zhenyu, "Physical modeling of reconfigurable intelligent surface for channel modeling," *China Commun.*, vol. 22, no. 2, pp. 128–142, Feb. 2025, IEEE.

[15] S. W. Ellingson, "Path loss in reconfigurable intelligent surface-enabled channels," in *Proc. IEEE PIMRC Symp.*, Sep. 2021.

[16] J. Hu, H. Yin, L. Tan, L. Cao, and X. Pei, "RIS-aided wireless communications: Can RIS beat flat metal plate?" *IEEE Trans. Veh. Technol.*, vol. 73, no. 10, pp. 15 704–15 708, Oct. 2024.

[17] E. Björnson, Ö. T. Demir, and L. Sanguinetti, "A primer on near-field beamforming for arrays and reconfigurable intelligent surfaces," in *Proc. ACSSC Conf.*, Nov. 2021, IEEE.

[18] P. Pouliguen and L. Desclos, "A physical optics approach to near field RCS computations," *Springer Ann. Telecom.*, vol. 51, no. 5, May 1996.

[19] R. Deban, H. Boutayeb, K. Wu, and J. Conan, "Deterministic approach for spatial diversity analysis of radar systems using near-field radar cross section of a metallic plate," *IEEE Trans. Antennas Propag.*, vol. 58, no. 3, pp. 908–916, Dec. 2010.

[20] P. Pouliguen, J. F. Damiens, R. Hemon, and J. Saillard, "RCS computation in near field," in *Proc. Days on Diffraction Conf.*, May 2006, IEEE.

[21] S. Häger, J. Ferreira, S. Böcker, D. Schreurs, and C. Wietfeld, "Passive intelligent reflecting surfaces for efficient 6G mmWave networks: Design, validation, and field trials," *IEEE Open J. Commun. Soc.*, pp. 1–27, 2026, submitted on 2025-12-23.

[22] J. Ferreira, A. Leßmann, D. Schreurs, and C. N. Manchón, "An empirical wideband performance analysis of mmWave passive RIS and reflectors," in *Proc. IEEE PIMRC Symp.*, Sep. 2025.